



HAL
open science

Application of asymptotic analysis to the two-scale modeling of small defects in mechanical structures

Eduard Mareníć, Delphine Brancherie, Marc Bonnet

► **To cite this version:**

Eduard Mareníć, Delphine Brancherie, Marc Bonnet. Application of asymptotic analysis to the two-scale modeling of small defects in mechanical structures. *International Journal of Solids and Structures*, 2017, 128, pp.199-209. 10.1016/j.ijsolstr.2017.08.029 . hal-01588407

HAL Id: hal-01588407

<https://hal.science/hal-01588407>

Submitted on 15 Sep 2017

HAL is a multi-disciplinary open access archive for the deposit and dissemination of scientific research documents, whether they are published or not. The documents may come from teaching and research institutions in France or abroad, or from public or private research centers.

L'archive ouverte pluridisciplinaire **HAL**, est destinée au dépôt et à la diffusion de documents scientifiques de niveau recherche, publiés ou non, émanant des établissements d'enseignement et de recherche français ou étrangers, des laboratoires publics ou privés.

Application of asymptotic analysis to the two-scale modeling of small defects in mechanical structures

Eduard Marenic^{a,1}, Delphine Brancherie^a, Marc Bonnet^{b,*}

^a*Université de Compiègne, Laboratoire Roberval
Centre de Recherches de Royallieu, CS60319, 60203 Compiègne, France*
^b*Unité de Mathématiques Appliquées, ENSTA, POems
828 boulevard des Marechaux, 91120 Palaiseau, France*

Abstract

This work aims at designing a numerical strategy towards assessing the nocivity of a small defect in terms of its size and position in a structure, at low computational cost, using only a mesh of the defect-free reference structure. The modification of the fields induced by the presence of a small defect is taken into account by using asymptotic corrections of displacements or stresses. This approach helps determining the potential criticality of defects by considering trial micro-defects with varying positions, sizes and mechanical properties, taking advantage of the fact that parametric studies on defect characteristics become feasible at virtually no extra computational cost. The proposed treatment is validated and demonstrated on two numerical examples involving 2D elastic configurations.

Keywords: asymptotic analysis, elastic moment tensor, defect, inhomogeneity.

1. Introduction

The role played by defects in the onset and development of rupture is crucial and has to be taken into account in order to assess the potential failure of mechanical structures. Difficulties in this context include (i) the length scale of defects often being much smaller than the structure length scale, and (ii) the frequent randomness of the location, nature and geometry of defects. Even with deterministic approaches, taking such defects into consideration by standard methods entails geometrical discretizations at the defect scale, leading to costly computations and hindering parametric studies for varying defect location and characteristics.

We address situations that require modeling a single small flaw, or a moderate number of such flaws, and therefore do not pertain to homogenization. Such isolated defects are usually either omitted (if small enough) or fully modelled. In the former case, initiation and eventual propagation of cracks leading to failure may be missed, while the latter case both complicates finite element (FE) model preparation and significantly increases computational costs due to severe mesh refinement in the region surrounding a modelled flaw.

*Corresponding author. E-mail address: mbonnet@ensta.fr

¹Current address: Institut Clément Ader, CNRS UMR 5312, Université Fédérale Toulouse Midi-Pyrénées, INSA/UPS/Mines Albi/ISAE 3 rue Caroline Aigle, 31 400 Toulouse, France.

In this work, we propose to address the latter issues by resorting to an efficient two-scale numerical strategy which can accurately predict the mechanical state perturbation caused by isolated inhomogeneities embedded in an elastic (background) material, without directly modeling them. To ensure computational efficiency, the analysis uses only a FE mesh for the defect-free structure, whose mesh size is hence not influenced by the (small) defect scale. The latter is instead taken into account by means of an asymptotic expansion, as previously done in [1, 2, 3] for modeling surface-breaking void defects (see also [4] where the concept of topological derivative [5, 6, 7] is used for predicting the eventual nocivity of surface-breaking small cracks). Here we are addressing the case of a small internal inhomogeneity (or a finite number thereof) embedded in an elastic solid. This includes traction-free voids as a special case, thus covering (small) objects variously referred to in the literature (see e.g. [8, 9, 10]) as inhomogeneities, heterogeneities, cracks, holes, porosities, inclusions... We rely on existing results on small-inhomogeneity asymptotics for elastic solids [11, 12, 13, 14, 6, 7], which prominently involve *elastic moment tensors* (EMTs) associated with elastic inhomogeneities [11, 12, 6], and combine them into a simple computational treatment, whose capabilities (prominently among them the ability to conduct inexpensive parametric studies) are then demonstrated on two examples.

The paper is organized as follows. After defining the relevant background and transmission problems (Sec. 2), the small-inhomogeneity asymptotic expansion in terms of the displacement perturbation is introduced, focusing on the far field, in Section 3. Therein, the key ingredients for its evaluation (elastostatic Green's tensor and EMT) are surveyed, and the resulting proposed computational treatment is given. Two validation and demonstration examples are then presented in Section 4. Section 5 closes the paper with concluding remarks and directions for future work.

2. Problem definition

We consider a linearly elastic body occupying a bounded domain $\Omega \subset \mathbb{R}^d$ (where $d = 2$ or 3 is the spatial dimensionality), whose boundary Γ is partitioned as $\Gamma = \Gamma_D \cup \Gamma_N$, with $\Gamma_D \cap \Gamma_N = \emptyset$ to ensure well-posedness of boundary value problems. The parts Γ_D and Γ_N respectively support a prescribed traction $\bar{\mathbf{t}}$ and a prescribed displacement $\bar{\mathbf{u}}$, while a body force density \mathbf{f} is applied in Ω . These boundary conditions are chosen for definiteness, and any other set of well-posed boundary conditions could be chosen instead with minimal changes. On the basis of this fixed geometrical and loading configuration, we consider

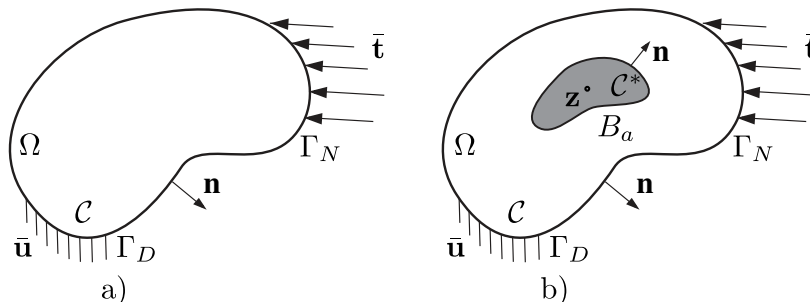


Figure 1: Reference (a) and perturbed (b) solids. The inhomogeneity B_a located at \mathbf{z} is the shaded subdomain in (b). 2

two situations, namely (i) a reference solid characterized by a given elasticity tensor \mathbf{C} , which defines the background solution, and (ii) a perturbed solid constituted of the same background material except for a small inhomogeneity whose material is characterized by the elasticity tensor \mathbf{C}^* . The aim of this work is to formulate a computational approach allowing to treat case (ii) as a perturbation of the background solution (i), in particular avoiding any meshing at the small inhomogeneity scale. This will be achieved by applying known results on the asymptotic expansion of the displacement perturbation with respect to the small characteristic size a of the inhomogeneity to case (ii).

2.1. Background solution (case (i))

The background solution in terms of displacement field \mathbf{u} arising in the reference solid Ω with elasticity tensor \mathbf{C} (Fig. 1a) due to prescribed excitation $(\mathbf{f}, \bar{\mathbf{t}}, \bar{\mathbf{u}})$, corresponding to case (i) above, solves the problem

$$\operatorname{div}(\mathbf{C} : \boldsymbol{\varepsilon}[\mathbf{u}]) + \mathbf{f} = \mathbf{0} \text{ in } \Omega, \quad \mathbf{t}[\mathbf{u}] = \bar{\mathbf{t}} \text{ on } \Gamma_N, \quad \mathbf{u} = \bar{\mathbf{u}} \text{ on } \Gamma_D, \quad (1)$$

where the linearized strain tensor $\boldsymbol{\varepsilon}[\mathbf{w}]$ and the traction vector $\mathbf{t}[\mathbf{w}]$ associated with a given displacement \mathbf{w} are given by

$$(a) \quad \boldsymbol{\varepsilon}[\mathbf{w}] = (\nabla \mathbf{w} + \nabla^T \mathbf{w})/2, \quad (b) \quad \mathbf{t}[\mathbf{w}] = (\mathbf{C} : \boldsymbol{\varepsilon}[\mathbf{w}]) \cdot \mathbf{n}, \quad (2)$$

with \mathbf{n} denoting the unit outward normal to Γ . In (2b) and hereinafter, symbols \cdot and $\cdot\cdot$ denote single and double inner products.

2.2. Transmission problem for a small inhomogeneity (case (ii))

The elastic body occupies the same domain Ω but now contains a small defect, in the form of an inhomogeneity located at $\mathbf{z} \in \Omega$, embedded in the background material (Fig. 1b). The inhomogeneity occupies the domain $B_a := \mathbf{z} + a\mathcal{B}$, where the smooth fixed domain $\mathcal{B} \subset \mathbb{R}^d$ centered at the origin defines the defect shape, and has elastic properties described by the tensor \mathbf{C}^* . The inhomogeneous elastic properties of the whole perturbed solid are therefore defined as

$$\mathbf{C}_a := \mathbf{C} + \Delta \mathbf{C} \chi_{B_a}, \quad (3)$$

where χ_D is the characteristic function of a domain D and $\Delta \mathbf{C} := \mathbf{C}^* - \mathbf{C}$ denotes the elasticity tensor perturbation.

The displacement field \mathbf{u}_a arising in the solid containing the small inhomogeneity B_a due to the same prescribed excitation $(\mathbf{f}, \bar{\mathbf{t}}, \bar{\mathbf{u}})$, solves the transmission problem

$$\begin{aligned} \operatorname{div}(\mathbf{C}_a : \boldsymbol{\varepsilon}[\mathbf{u}_a]) + \mathbf{f} = \mathbf{0} \text{ in } B_a \cup (\Omega \setminus \overline{B_a}), \quad \mathbf{t}[\mathbf{u}_a] = \bar{\mathbf{t}} \text{ on } \Gamma_N, \quad \mathbf{u}_a = \bar{\mathbf{u}} \text{ on } \Gamma_D, \\ \mathbf{u}_a|_- = \mathbf{u}_a|_+ \quad \text{and} \quad \mathbf{t}^*[\mathbf{u}_a]|_- = \mathbf{t}[\mathbf{u}_a]|_+ \quad \text{on } \partial B_a, \end{aligned} \quad (4)$$

where the traction operator \mathbf{t}^* is defined by (2b) with \mathbf{C} replaced by \mathbf{C}^* and the \pm subscripts indicate traces relative to B_a and $\Omega \setminus \overline{B_a}$, respectively.

3. Computation of small-inhomogeneity solution asymptotics

This section develops our proposed methodology. The small-inhomogeneity asymptotic expansion in terms of the displacement perturbation is introduced, focusing on the far field,

in Sec. 3.1. The key ingredients for its evaluation, namely the elastostatic Green's tensor and elastic moment tensors, are surveyed in Secs. 3.2 and 3.3, respectively, the resulting proposed computational treatment being then given in Sec. 3.4. Some useful explicit formulas for the plane strain case are finally gathered in Sec. 3.5.

3.1. Asymptotic approximation of displacement perturbation

We begin by introducing the displacement perturbation

$$\mathbf{v}_a := \mathbf{u}_a - \mathbf{u}, \quad (5)$$

where \mathbf{u}_a and \mathbf{u} solve problems (4) and (1), respectively corresponding to the perturbed and background configurations. An asymptotic analysis of \mathbf{v}_a with respect to the characteristic defect size a provides a way to evaluate the influence of the location, size, shape and material characteristics of defects on the solution \mathbf{u}_a . Available asymptotic approximations, such as those used in this work, nearly always rely on a constitutive linearity assumption (here, linear elasticity), with the notable exception of [15].

Two kinds of asymptotic expansions of \mathbf{v}_a may be defined, namely *inner* and *outer* expansions [16]. They focus on the two scales involved: (a) the structure scale, where points are described using "ordinary" coordinates $\mathbf{x} \in \Omega$, and (b) the defect scale corresponding to the characteristic length a of the inhomogeneity, with rescaled coordinates $\bar{\mathbf{x}} := (\mathbf{x} - \mathbf{z})/a$. This description is directly related to the slow and fast variables used in [1, 2].

Inner expansion. The inner expansion has the form [17], [6, Prop. 3.2]

$$\mathbf{v}_a(\mathbf{x}) = a\mathbf{v}_B[\mathbf{E}](\bar{\mathbf{x}}) + o(a), \quad \mathbf{E} = \nabla\mathbf{u}(\mathbf{z}), \quad (6)$$

having set $\mathbf{v}_B[\mathbf{E}] := \mathbf{u}_B[\mathbf{E}] - \mathbf{E} \cdot \bar{\mathbf{x}}$ in terms of the solution $\mathbf{u}_B[\mathbf{E}]$ of the *free-space transmission problem* (FSTP)

$$\begin{aligned} \operatorname{div}(\mathbf{C}^* : \boldsymbol{\varepsilon}[\mathbf{u}_B]) &= \mathbf{0} \quad \text{in } \mathbb{R}^d \setminus \bar{\mathcal{B}}, & \operatorname{div}(\mathbf{C} : \boldsymbol{\varepsilon}[\mathbf{u}_B]) &= \mathbf{0} \quad \text{in } \mathcal{B}, \\ |\mathbf{u}_B(\bar{\mathbf{x}}) - \mathbf{E} \cdot \bar{\mathbf{x}}| &\rightarrow 0 \quad \text{for } |\bar{\mathbf{x}}| \rightarrow \infty, & & \\ \mathbf{u}_B|_- &= \mathbf{u}_B|_+ \quad \text{and} \quad \mathbf{t}^*[\mathbf{u}_B]|_- &= \mathbf{t}[\mathbf{u}_B]|_+ \quad \text{on } \partial\mathcal{B}, \end{aligned} \quad (7)$$

i.e. the auxiliary problem of a perfectly bonded inhomogeneity \mathcal{B} embedded in an infinite elastic medium and subjected to the constant remote stress $\mathbf{C} : \mathbf{E}$ for given $\mathbf{E} \in \mathbb{R}_{\text{sym}}^{d \times d}$. Such solutions \mathbf{v}_B are known analytically for simple inhomogeneity shapes [10], in terms of the solution to the famous Eshelby inclusion problem [18]. Expansion (6) essentially effects a zoom at the inhomogeneity scale a ; it is expressed in terms of the fast coordinates $\bar{\mathbf{x}}$, and is valid for finite $\bar{\mathbf{x}}$, i.e. within a neighbourhood of B_a whose diameter is of order $O(a)$.

Outer expansion. The outer expansion, on the other hand, is given by [12, Thm. 11.4]

$$\mathbf{v}_a(\mathbf{x}) = -\nabla_{(1)}\mathbf{G}(\mathbf{z}, \mathbf{x}) : \mathcal{A}(\mathcal{B}, \mathbf{C}, \Delta\mathbf{C}) : \nabla\mathbf{u}(\mathbf{z})a^d + o(a^d), \quad \mathbf{x} \neq \mathbf{z}, \quad (8)$$

where \mathbf{G} is the elastostatic Green's tensor (defined next in Sec. 3.2), $\nabla_{(1)}\mathbf{G}$ denotes the gradient with respect to the first argument of the two-point function \mathbf{G} , and \mathcal{A} is the elastic moment tensor (EMT) associated with the inhomogeneity (Sec. 3.3). Expansion (8) is expressed in terms of the slow coordinates \mathbf{x} and is valid at any finite (independent on a) distance from the inhomogeneity, i.e. at the structure scale. Expansion matching techniques

then allow to blend inner and outer expansions into a unique expansion valid uniformly in Ω [16]; exploiting this approach is however left for future work.

Asymptotic correction. We study in this work the computation of the *asymptotic correction*

$$\tilde{\mathbf{v}}_a(\mathbf{x}) := -\nabla_{(1)}\mathbf{G}(\mathbf{z}, \mathbf{x}) : \mathcal{A}(\mathcal{B}, \mathcal{C}, \Delta\mathcal{C}) : \nabla\mathbf{u}(\mathbf{z})a^d \quad (9)$$

i.e. the leading contribution to the outer approximation (8). We will consider two computational scenarios, namely (a) fixed inclusion location \mathbf{z} and varying evaluation point \mathbf{x} , or (b) fixed evaluation point \mathbf{x} and varying inclusion location \mathbf{z} . The key ingredients of (9) are (i) $\nabla\mathbf{u}(\mathbf{z})$, the gradient of the background solution at the inhomogeneity location (or, equivalently, its strain or stress at that point), (ii) the gradient $\nabla_{(1)}\mathbf{G}(\mathbf{z}, \mathbf{x})$ of the Green's tensor \mathbf{G} , and (iii) the elastic moment tensor (EMT) \mathcal{A} . Ingredient (i) being a natural outcome of a FEM solution of the background problem (1), we focus on the definition and numerical evaluation of $\nabla_{(1)}\mathbf{G}(\mathbf{z}, \mathbf{x})$ and \mathcal{A} .

3.2. Elastostatic Green's tensor

3.2.1. Definition and symmetry properties

The elastostatic Green's tensor appearing in (8) and (9) is defined as $\mathbf{G}(\boldsymbol{\xi}, \mathbf{x}) = \mathbf{e}_k \otimes \mathbf{G}^k(\boldsymbol{\xi}, \mathbf{x})$, where the displacement field $\mathbf{G}^k(\boldsymbol{\xi}, \mathbf{x})$ is the response at $\boldsymbol{\xi} \in \Omega$ of the background body subjected to (i) a unit point force applied at $\mathbf{x} \in \Omega$ along the coordinate direction \mathbf{e}_k and (ii) homogeneous boundary conditions, i.e.:

$$\begin{aligned} -\operatorname{div}(\mathcal{C} : \boldsymbol{\varepsilon}[\mathbf{G}^k(\cdot, \mathbf{x})]) &= \delta(\cdot - \mathbf{x})\mathbf{e}_k && \text{in } \Omega, \\ \mathbf{t}[\mathbf{G}^k(\cdot, \mathbf{x})] &= \mathbf{0} && \text{on } \Gamma_N \quad (1 \leq k \leq d) \quad (10) \\ \mathbf{G}^k(\cdot, \mathbf{x}) &= \mathbf{0} && \text{on } \Gamma_D, \end{aligned}$$

where δ denotes the unit Dirac mass at the coordinate origin. In the above definition, and wherever component notation is used, Einstein's summation convention over repeated indices implicitly applies.

Symmetry relations. The elastostatic Green's tensor verifies the symmetry relationship

$$\mathbf{G}(\mathbf{z}, \mathbf{x}) = \mathbf{G}^T(\mathbf{x}, \mathbf{z}), \quad \text{i.e. } G_i^k(\mathbf{z}, \mathbf{x}) = G_k^i(\mathbf{x}, \mathbf{z}), \quad (11a)$$

(for a proof, apply Maxwell-Betti's reciprocity theorem to the displacement fields $\mathbf{G}^k(\cdot, \mathbf{x})$ and $\mathbf{G}^i(\cdot, \mathbf{z})$ in the domain Ω , recalling that they are elastic solutions for unit point forces $\delta(\cdot - \mathbf{x})\mathbf{e}_k$ and $\delta(\cdot - \mathbf{z})\mathbf{e}_i$, respectively, and that they satisfy identical homogeneous boundary conditions on Γ). Relationships (11a) hold for any $(\mathbf{x}, \mathbf{z}) \in \Omega \times \Omega$, $\mathbf{x} \neq \mathbf{z}$. Writing them for $(\mathbf{x} + d\mathbf{x}, \mathbf{z} + d\mathbf{z}) \in \Omega \times \Omega$ and extracting first-order contributions in $d\mathbf{x}$, $d\mathbf{z}$, we have

$$\nabla_{(1)}G_i^k(\mathbf{z}, \mathbf{x}) \cdot d\mathbf{z} + \nabla_{(2)}G_i^k(\mathbf{z}, \mathbf{x}) \cdot d\mathbf{x} = \nabla_{(1)}G_k^i(\mathbf{x}, \mathbf{z}) \cdot d\mathbf{x} + \nabla_{(2)}G_k^i(\mathbf{x}, \mathbf{z}) \cdot d\mathbf{z}$$

for all $d\mathbf{x}$, $d\mathbf{z}$, implying the symmetry relationship

$$\nabla_{(1)}G_i^k(\mathbf{z}, \mathbf{x}) = \nabla_{(2)}G_k^i(\mathbf{x}, \mathbf{z}) \quad (\mathbf{x}, \mathbf{z}) \in \Omega \times \Omega \text{ with } \mathbf{x} \neq \mathbf{z}, \quad 1 \leq i, k \leq d. \quad (11b)$$

3.2.2. Decomposition of \mathbf{G}

We now introduce the following additive decomposition of \mathbf{G} :

$$\mathbf{G}(\cdot, \mathbf{x}) = \mathbf{G}_\infty(\cdot - \mathbf{x}) + \mathbf{G}_c(\cdot, \mathbf{x}), \quad (12)$$

where \mathbf{G}_∞ is the (singular) full-space Green's tensor (also called fundamental tensor), while the complementary (non-singular) tensor \mathbf{G}_c is defined in order for \mathbf{G} to satisfy the homogeneous boundary conditions of problem (10). Decomposition (12) allows to exploit the fact that the fundamental tensor $\mathbf{G}_\infty = \mathbf{e}_k \otimes \mathbf{G}_\infty^k$ is known analytically. Indeed, the displacement field \mathbf{G}_∞^k ($1 \leq k \leq d$) arising from a unit point force applied along direction k at the origin, which satisfies

$$\operatorname{div}(\mathbf{C} : \boldsymbol{\varepsilon}[\mathbf{G}_\infty^k]) + \delta \mathbf{e}_k = \mathbf{0} \quad \text{in } \mathbb{R}^d,$$

is given for an arbitrary anisotropic background material (up to arbitrary translations if $d = 2$) by the Fourier integral [10]

$$\mathbf{G}_\infty(\mathbf{x}) = \frac{1}{(2\pi)^d} \int_{\mathbb{R}^d} \exp(i\boldsymbol{\eta} \cdot \mathbf{x}) \mathbf{N}(\boldsymbol{\eta}) \, dV(\boldsymbol{\eta}), \quad \mathbf{x} \in \mathbb{R}^3 \setminus \{\mathbf{0}\}, \quad (13)$$

where, for given $\boldsymbol{\eta} \in \mathbb{R}^3$, the second-order tensor $\mathbf{N}(\boldsymbol{\eta})$ is given by

$$\mathbf{N}(\boldsymbol{\eta}) = \mathbf{K}^{-1}(\boldsymbol{\eta}), \quad K_{ik}(\boldsymbol{\eta}) = \mathcal{C}_{ijkl} \eta_j \eta_l \quad (14)$$

(note that $\mathbf{K}(\boldsymbol{\eta})$, known as the acoustic tensor or the Christoffel tensor, is indeed invertible for any $\boldsymbol{\eta} \neq \mathbf{0}$ by virtue of \mathbf{C} being positive definite). The tensor field \mathbf{G}_∞ is singular at $\mathbf{x} = \mathbf{0}$ (the order of singularity is well-known to be $O(|\mathbf{x}|^{-1})$ for $d = 3$ or $O(\ln|\mathbf{x}|)$ for $d = 2$, and can be deduced from the representation (13)). It is also clearly invariant under translations, i.e. unit point forces applied at $\mathbf{x} \in \mathbb{R}^d$ generate displacements $\mathbf{G}_\infty(\boldsymbol{\xi} - \mathbf{x})$ at $\boldsymbol{\xi} \in \mathbb{R}^d$. If the background material is isotropic, the Fourier integral (13) can be evaluated in closed form, yielding Kelvin's solution (see Sec. 3.5 for the plane strain case).

The symmetry relations (11a,b) hold for $\mathbf{G}(\cdot, \mathbf{x})$ replaced with $\mathbf{G}_\infty(\cdot - \mathbf{x})$, which in fact possesses additional symmetry properties and satisfies

$$\mathbf{G}_\infty(\boldsymbol{\xi} - \mathbf{x}) = \mathbf{G}_\infty(\mathbf{x} - \boldsymbol{\xi}) = \mathbf{G}_\infty^T(\mathbf{x} - \boldsymbol{\xi}), \quad (15a)$$

$$\partial_\xi \mathbf{G}_\infty(\boldsymbol{\xi} - \mathbf{x}) = \nabla \mathbf{G}_\infty(\boldsymbol{\xi} - \mathbf{x}) = -\nabla \mathbf{G}_\infty(\mathbf{x} - \boldsymbol{\xi}). \quad (15b)$$

Properties (11a,b) and (15a,b) will play an important role in the actual evaluation of the asymptotic correction (9).

3.2.3. Complementary Green's tensor

The second part of decomposition (12) namely the complementary part $\mathbf{G}_c = \mathbf{e}_k \otimes \mathbf{G}_c^k$ of the Green's tensor, is the correction applied to \mathbf{G}_∞ due to the finite size of Ω , and is bounded at $\boldsymbol{\xi} = \mathbf{x}$. More precisely, by virtue of problem (10) being linear, each \mathbf{G}_c^k ($1 \leq k \leq d$) solves the following elastostatic boundary-value problem (BVP) with regular boundary data and vanishing zero body force density:

$$\begin{aligned} \operatorname{div}(\mathbf{C} : \boldsymbol{\varepsilon}[\mathbf{G}_c^k(\cdot, \mathbf{x})]) &= \mathbf{0} && \text{in } \Omega, \\ \mathbf{G}_c^k(\cdot, \mathbf{x}) &= -\mathbf{G}_\infty^k(\cdot - \mathbf{x}) && \text{on } \Gamma_D, \\ \mathbf{t}[\mathbf{G}_c^k(\cdot, \mathbf{x})] &= -\mathbf{t}[\mathbf{G}_\infty^k(\cdot - \mathbf{x})] && \text{on } \Gamma_N. \end{aligned} \quad (16)$$

implying that $\mathbf{G}_c^k(\boldsymbol{\xi}, \mathbf{x})$ is C^∞ for $\boldsymbol{\xi}, \mathbf{x} \in \Omega$. Problem (16) involves \mathbf{G}_∞^k and its derivatives on Γ , with the traction operator $\mathbf{t}[\cdot]$ still defined by (2b); all these quantities are known analytically, in closed form if the background medium is isotropic (see Sec. 3.5).

To evaluate $\nabla_{(1)}\mathbf{G}(\mathbf{z}, \mathbf{x})$ used in the asymptotic correction (9), it seems natural to solve numerically problem (16) for \mathbf{G}_c^k ($1 \leq k \leq d$) and then compute $\nabla_{(1)}\mathbf{G}(\mathbf{z}, \mathbf{x}) = \nabla\mathbf{G}_\infty(\mathbf{z}-\mathbf{x}) + \nabla_{(1)}\mathbf{G}_c(\mathbf{z}, \mathbf{x})$. However, while $\nabla\mathbf{G}_\infty$ is known analytically (see (28) for the plane strain case), $\nabla\mathbf{G}_c$ must in general be evaluated via numerical differentiation of the computed solution for \mathbf{G}_c , a step which is likely to entail loss of accuracy. Moreover, solving (16) for given \mathbf{x} allows to evaluate $\tilde{\mathbf{v}}_a$ via (9) for a fixed evaluation point \mathbf{x} and varying inhomogeneity locations \mathbf{z} , i.e. is convenient for scenario (b) but potentially costly for scenario (a) (with scenarios as defined after Eq. (9)). We therefore propose two distinct strategies for the evaluation of $\nabla_{(1)}\mathbf{G}$, according to whether scenario (a) or (b) is to be considered.

Case (a): fixed flaw location and varying evaluation point. For this situation, solving problem (16) for each evaluation point \mathbf{x} would incur significant computational costs. We propose an alternative approach, which consists in finding a governing elasticity problem for $\nabla_{(1)}\mathbf{G}(\mathbf{z}, \cdot)$ with \mathbf{z} fixed. We begin by using the symmetry relationship (11a) in (9), so as to swap the roles of \mathbf{x} and \mathbf{z} , to obtain (in component form)

$$\begin{aligned} [\tilde{v}_a]_k(\mathbf{x}) &= -\partial_{(1)j}G_i^k(\mathbf{z}, \mathbf{x})\mathcal{A}_{ijmn}u_{m,n}(\mathbf{z})a^d \\ &= -\partial_{(2)j}G_k^i(\mathbf{x}, \mathbf{z})\mathcal{A}_{ijmn}u_{m,n}(\mathbf{z})a^d \end{aligned} \quad (17)$$

with notations $\partial_{(1)j}$ and $\partial_{(2)j}$, respectively, indicating partial differentiation with respect to the j -th coordinate of the first and second argument of \mathbf{G} . Now, decomposition (12) implies

$$G_k^i(\cdot, \mathbf{z}) = [G_\infty^i]_k(\cdot - \mathbf{z}) + [G_c^i]_k(\cdot, \mathbf{z}), \quad (18)$$

where $\mathbf{G}_c^i(\cdot, \mathbf{z})$ is governed by problem (16) with \mathbf{x} replaced by \mathbf{z} and k by i . Moreover, $\nabla_{(2)}\mathbf{G}_c$ may be defined by simply differentiating the BVP (16) with respect to the second argument of \mathbf{G}_c , which acts in (16) as a parameter, and solving the resulting derivative BVP for $\nabla_{(2)}\mathbf{G}_c$. Accordingly, each displacement field $\mathbf{H}_j^i(\cdot, \mathbf{z}) := \partial_{(2)j}\mathbf{G}_c^i(\cdot, \mathbf{z})$ ($1 \leq i, j \leq d$) solves the BVP

$$\begin{aligned} \operatorname{div}(\mathbf{C} : \varepsilon[\mathbf{H}_j^i(\cdot, \mathbf{z})]) &= \mathbf{0} && \text{in } \Omega, \\ \mathbf{H}_j^i(\cdot, \mathbf{z}) &= \partial_{(1)j}\mathbf{G}_\infty^i(\cdot, \mathbf{z}) && \text{on } \Gamma_D, \\ \mathbf{t}[\mathbf{H}_j^i(\cdot, \mathbf{z})] &= \mathbf{t}[\partial_{(1)j}\mathbf{G}_\infty^i(\cdot, \mathbf{z})] && \text{on } \Gamma_N. \end{aligned} \quad (19)$$

Explicit formulas for the boundary data in problems (19) are given in Sec. 3.5 for the case of isotropy and plain strain, see Eqs. (28) and (29). Then, the asymptotic correction $\tilde{\mathbf{v}}_a$ can be evaluated using

$$\tilde{\mathbf{v}}_a(\mathbf{x}) = \tilde{\mathbf{v}}_{a,\infty}(\mathbf{x}) + \tilde{\mathbf{v}}_{a,c}(\mathbf{x}) =: (\partial_{(1)j}\mathbf{G}_\infty^i(\mathbf{x} - \mathbf{z}) - \mathbf{H}_j^i(\mathbf{x}, \mathbf{z}))\mathcal{A}_{ijmn}u_{m,n}(\mathbf{z})a^d \quad (20)$$

(having introduced in (17) the Green's tensor decomposition (18), and used (15b) for \mathbf{G}_∞). Evaluating the above expression *a priori* entails numerically solving the d^2 problems (19), which are set on the unperturbed (defect-free) configuration.

Case (b): varying flaw location and fixed evaluation point. For this situation, it seems impossible to derive a problem similar to (19) whose unknown is $\partial_{(1)j}G_i^k(\cdot, \mathbf{x})$ or $\partial_{(2)j}G_k^i(\mathbf{x}, \cdot)$, with \mathbf{x} fixed, because the partial derivative $\partial_{(1)j}$ or $\partial_{(2)j}$ now acts on the field point rather than the source point, and differentiating the boundary conditions in (16) w.r.t. the field point will not yield the correct boundary conditions for the problem governing $\partial_{(1)j}G_i^k(\cdot, \mathbf{x})$ or $\partial_{(2)j}G_k^i(\mathbf{x}, \cdot)$ (whereas, as done previously, differentiating the BCs in (16) w.r.t. the source point is valid). Consequently:

- (i) For computing displacement corrections of the form (17), one may solve problems (16) and differentiate the resulting numerical solution (e.g. by differentiating the finite element approximation).
- (ii) For computing strain or stress corrections, requiring derivatives of (17), one notes that

$$\begin{aligned}\partial_\ell [\tilde{v}_a]_k(\mathbf{x}) &= -\partial_{(2)\ell}\partial_{(1)j}G_i^k(\mathbf{z}, \mathbf{x})\mathcal{A}_{ijmn}u_{m,n}(\mathbf{z})a^d \\ &= -\partial_{(1)j}[H_\ell^k(\mathbf{z}, \mathbf{x})]_i\mathcal{A}_{ijmn}u_{m,n}(\mathbf{z})a^d\end{aligned}\quad (21)$$

Such evaluations may therefore be effected by solving problem (19) with $\mathbf{z} = \mathbf{x}$ (i.e. the source point for problem (19) set equal to the fixed evaluation point \mathbf{x}), and then differentiating the resulting numerical solution for $H_\ell^k(\cdot, \mathbf{x})$.

To understand the BC differentiation w.r.t. field point issue, consider as an example the function $u(x, y) = x^2 + y^2 - 1$ solving $\Delta u = 4$ in D and $u = 0$ on ∂D , D being the unit disk. The partial derivative $w := \partial_x u = 2x$ solves $\Delta w = 0$ in D (i.e. the field equation is the derivative of the original field equation); however the boundary data $w = 2x$ on ∂D cannot be inferred from the original problem, since u needs for this to be known at least in a neighbourhood of ∂D .

3.3. Elastic moment tensor

The EMT \mathcal{A} associated with an inhomogeneity of shape \mathcal{B} and stiffness \mathcal{C}^* embedded in a background medium of stiffness \mathcal{C} is defined by

$$\mathcal{A} : \mathbf{E} = \int_{\mathcal{B}} \Delta \mathcal{C} : \nabla \mathbf{u}_{\mathcal{B}}[\mathbf{E}] \, dV, \quad \forall \mathbf{E} \in \mathbb{R}_{\text{sym}}^{d \times d}, \quad (22)$$

where $\mathbf{u}_{\mathcal{B}}[\mathbf{E}]$ solves the FSTP (7). The EMT carries important microstructural information, as it depends on the material properties $\mathcal{C}, \mathcal{C}^*$ and, through \mathcal{B} , on the inhomogeneity shape and orientation.

Main properties. The EMT (22) has the following known properties [11, 6, 14]:

1. Symmetry: \mathcal{A} has major and minor symmetries;
2. Scaling: $\mathcal{A}(\lambda \mathcal{B}, \mathcal{C}, \mathcal{C}^*) = \lambda^d \mathcal{A}(\mathcal{B}, \mathcal{C}, \mathcal{C}^*)$ for any $\lambda > 0$;
3. Sign: \mathcal{A} is positive definite (resp. negative definite) if all solutions Λ of the eigenvalue problem $(\Delta \mathcal{C} - \Lambda \mathcal{C}) : \mathbf{E} = \mathbf{0}$ are positive (resp. negative), i.e. if the inhomogeneity is stiffer (resp. softer) than the background.

On examining (20) in light of the minor symmetry of \mathcal{A} , we find that solving the $d(d+1)/2$ problems (19) for $1 \leq i \leq j \leq d$, instead of the d^2 problems for all i, j , is sufficient.

EMT for an ellipsoidal inhomogeneity. When \mathcal{B} is an ellipsoid, $\nabla \mathbf{u}_{\mathcal{B}}[\mathbf{E}]$ is constant inside \mathcal{B} [18, 10], allowing \mathcal{A} to be expressed in closed form [11, 6]:

$$\mathcal{A} = |\mathcal{B}| \mathcal{C} : (\mathcal{C} + \Delta \mathcal{C} : \mathcal{S})^{-1} : \Delta \mathcal{C}, \quad (23)$$

where $\mathcal{S} = \mathcal{S}(\mathcal{B}, \mathcal{C})$ denotes the (fourth-order) Eshelby tensor of the normalized inclusion \mathcal{B} . The evaluation of \mathcal{A} then essentially rests on that of \mathcal{S} . In the general anisotropic case, the Cartesian components of \mathcal{S} in an orthonormal frame aligned with the principal directions of \mathcal{B} are given in the three-dimensional case by [10]

$$\mathcal{S}_{ijkl} = \frac{1}{8\pi} \mathcal{C}_{mnkl} \int_{\Sigma} [\eta_j N_{im}(\boldsymbol{\eta}) + \eta_i N_{jm}(\boldsymbol{\eta})] \eta_n \, dS(\hat{\boldsymbol{\eta}}), \quad (24)$$

where $\Sigma := \{\hat{\boldsymbol{\eta}} \in \mathbb{R}^3, |\hat{\boldsymbol{\eta}}| = 1\}$ is the unit sphere, $\boldsymbol{\eta} := a_1^{-1} \hat{\eta}_1 \mathbf{e}_1 + a_2^{-1} \hat{\eta}_2 \mathbf{e}_2 + a_3^{-1} \hat{\eta}_3 \mathbf{e}_3$, (a_1, a_2, a_3 being the principal semiaxes of \mathcal{B}), and \mathbf{N} is defined by (14). A similar formula holds for the plane-strain case. Evaluation of (24) in general requires numerical quadrature (see e.g. [6, 19]). When \mathcal{C} is isotropic, the formula (24) can be evaluated analytically in closed form.

3.4. Computational procedure

The considerations of Secs. 3.1 to 3.3 translate into a computational procedure allowing an efficient evaluation of the asymptotic correction $\tilde{\mathbf{v}}_a$. The procedure can be decomposed into six steps, described next and summarized in Table 1. It requires finite element (FE) analyses using a mesh of the background solid (whose design does not involve the defect length scale), denoted M_H . The subscript H refer to the characteristic element size for this mesh; likewise, finite element solutions computed on this mesh (i.e. fields defined by nodal interpolation based on mesh M_H) will be labelled with a superscript H (e.g. \mathbf{u}^H).

In Step 1, we compute \mathbf{u}^H , the FE approximation on M_H of the background solution \mathbf{u} defined by problem (1). The subsequent steps 2 to 6 aim at correcting \mathbf{u}^H without meshing the inhomogeneity. As emphasized in Table 1, steps 2 to 4 only require the inhomogeneity position \mathbf{z} , while steps 5 and 6 also need the inhomogeneity properties.

For a given inhomogeneity position $\mathbf{z} \in \Omega$, we extract $\nabla \mathbf{u}^H(\mathbf{z})$, the gradient of the background displacement (step 2). Steps 3 and 4 then perform the computation of the gradient of the Green's tensor as given by decomposition (18). Step 3 uses the relevant derivatives

Table 1: Summary of the computational procedure for $\tilde{\mathbf{v}}_a^H$.

Step	Description	eq. number
1	compute \mathbf{u}^H	(1)
inhomogeneity position \mathbf{z}		
2	extract $\nabla \mathbf{u}^H(\mathbf{z})$	
3	evaluate $\nabla \mathbf{G}_{\infty}(\mathbf{x}, \mathbf{z})$ (prepare BC's for $\nabla \mathbf{G}_c$)	(28) (28), (29)
4	compute $[\mathbf{H}_j^i]^H$ for $1 \leq i \leq j \leq d$	(19)
inhomogeneity properties $\mathcal{B}, \mathcal{C}^*$		
5	evaluate $\mathcal{A}(\mathcal{B}, \mathcal{C}, \mathcal{C}^*)$	(23) or (24)
6	evaluate $\tilde{\mathbf{v}}_a^H$ and \mathbf{u}_a^H	(9), (25)

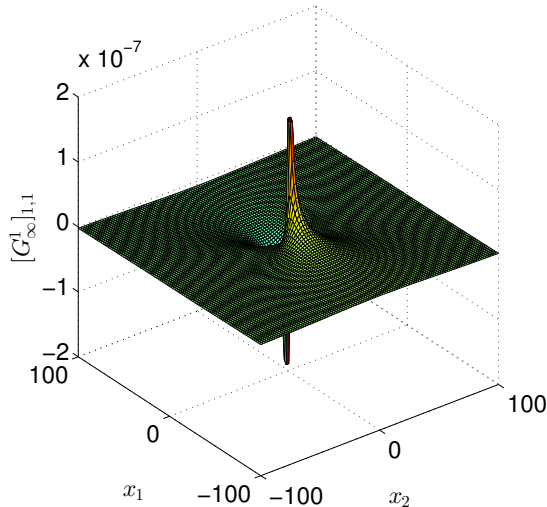


Figure 2: Plot of the component $\partial_{(1)1}[G_\infty^1]_1$ of \mathbf{G}_∞ , whose boundary trace is used in the BCs of problem (19).

of \mathbf{G}_∞ (see (28) and (29) for the plane strain case) for (i) evaluating the corresponding contribution to $\tilde{\mathbf{v}}_a$ in (9) and (ii) setting up the boundary data of problem (19). Clearly, special attention needs to be given to the preparation and correct imposition of these BCs. A surface plot of component $\partial_{(1)1}[G_\infty^1]_1$, used as boundary data in problem (19), is shown for illustration purposes in Fig. 2. Step 4 then effects the computation of finite element solutions $[\mathbf{H}_j^i]^H$ of the $d(d+1)/2$ problems (19) for $1 \leq i \leq j \leq d$.

Next, given the shape \mathcal{B} and material properties \mathbf{C}^* of the inhomogeneity, we compute in step 5 the EMT $\mathcal{A}(\mathcal{B}, \mathbf{C}, \Delta\mathbf{C})$ using (23). Finally, Step 6 completes the evaluation of $\tilde{\mathbf{v}}_a^H$ and the asymptotic approximation $\tilde{\mathbf{u}}_a^H$ of the transmission solution through

$$\tilde{\mathbf{v}}_a^H := \left(\partial_{(1)j}[\mathbf{G}_\infty^i]^H(\cdot - \mathbf{z}) - [\mathbf{H}_j^i]^H(\cdot, \mathbf{z}) \right) \mathcal{A}_{ijmn} u_{m,n}^H(\mathbf{z}) a^d, \quad \tilde{\mathbf{u}}_a^H := \mathbf{u}^H + \tilde{\mathbf{v}}_a^H. \quad (25)$$

It is important to note that the computation of EMT requires negligible effort, whereas simulating different inhomogeneities using fine meshes necessitates separate runs on fine meshes, each of which having to be prepared beforehand.

Multiple defects. Several defects B_a^ℓ ($1 \leq \ell \leq m$), with fixed locations \mathbf{z}^ℓ and diameters proportional to the same small length parameter a , can be considered simultaneously by simply setting $\tilde{\mathbf{v}}_a^H = \sum_\ell \tilde{\mathbf{v}}_a^{\ell,H}$ (where $\tilde{\mathbf{v}}_a^{\ell,H}$ is the asymptotic correction (25) for the ℓ -th defect considered in isolation), since terms coupling different defects occur only in higher-order contributions to inner or outer solution expansions (see e.g. [7]).

Varying defect characteristics. The structure of asymptotic correction formulas such as (25) greatly facilitates parametric studies for varying defect characteristics. All defect parameters except its location occur only in the EMT \mathcal{A} , so that varying the defect shape, orientation or material parameters only requires modifying \mathcal{A} . In addition, how to efficiently vary the defect location was addressed in Sec. 3.2.3. The ability to conduct inexpensive parametric studies is illustrated in the second example of Sec. 4.

3.5. The plane strain case

We collect here, for convenience, known explicit expressions for plane strain conditions of (i) the Kelvin fundamental solution and its relevant derivatives and (ii) the elastic moment tensor for an elliptical inhomogeneity, on which the numerical examples of Sec. 4 are based.

Green's tensor. Kelvin's fundamental displacement for plane strain conditions is given by

$$[G_\infty^i]_k(\mathbf{r}) = \frac{1}{8\pi\mu(1-\nu)} \left[\hat{r}_i \hat{r}_k - (3-4\nu)\delta_{ik} \ln \frac{r}{r'} \right] \quad \mathbf{r} \in \mathbb{R}^2 \setminus \{\mathbf{0}\}; \quad i, k = 1, 2 \quad (26)$$

where $r = |\mathbf{r}| = (\mathbf{r} \cdot \mathbf{r})^{1/2}$, $\hat{\mathbf{r}} = r^{-1}\mathbf{r}$, and r' denotes an arbitrary reference length. In this case, \mathbf{G}_∞ as given by (26) is in fact the response of a three-dimensional infinite body to an infinite line (passing through the origin and directed along \mathbf{e}_3) of unit point loads, see e.g. [20, 21], and is defined up to an arbitrary translation (defined by r'). Then, introducing (26) in Hooke's law yields Kelvin's stress tensor Σ_∞ , whose components are given by

$$[\Sigma_\infty^i]_{k\ell}(\mathbf{r}) = \frac{-1}{4\pi(1-\nu)r} [2\hat{r}_k \hat{r}_i \hat{r}_\ell + (1-2\nu)(\delta_{ik} \hat{r}_\ell + \delta_{i\ell} \hat{r}_k - \delta_{k\ell} \hat{r}_i)]. \quad (27)$$

The boundary data involved in the boundary conditions of problems (19) are then found by straightforward differentiation of (26) and (27):

$$\partial_{(1)j}[G_\infty^i]_k(\mathbf{x}, \mathbf{z}) = \frac{-1}{8\pi\mu(1-\nu)r} [2\hat{r}_i \hat{r}_j \hat{r}_k - \delta_{ij} \hat{r}_k - \delta_{kj} \hat{r}_i + (3-4\nu)\delta_{ik} \hat{r}_j], \quad (28)$$

$$\begin{aligned} \partial_{(1)j}[\Sigma_\infty^i]_{k\ell}(\mathbf{x}, \mathbf{z}) = & \frac{-1}{4\pi(1-\nu)r^2} \left[2(-4\hat{r}_i \hat{r}_j \hat{r}_k \hat{r}_\ell + \delta_{jk} \hat{r}_i \hat{r}_\ell + \delta_{j\ell} \hat{r}_i \hat{r}_k + \delta_{ij} \hat{r}_k \hat{r}_\ell) \right. \\ & + (1-2\nu)(-2(\delta_{ik} \hat{r}_j \hat{r}_\ell + \delta_{i\ell} \hat{r}_j \hat{r}_k - \delta_{k\ell} \hat{r}_i \hat{r}_j) \\ & \left. + \delta_{ik} \delta_{j\ell} + \delta_{i\ell} \delta_{jk} - \delta_{ij} \delta_{k\ell}) \right]. \quad (29) \end{aligned}$$

Elastic moment tensor. The Eshelby tensor for an elliptical inclusion \mathcal{B} in plane strain can be found from (24) by considering the limiting case of a 3D ellipsoidal inclusion infinitely elongated in the x_3 direction. Assuming \mathcal{C} to be isotropic, analytical evaluation of the 2D version of (24) yields the following explicit expressions for the nonzero Eshelby tensor components [10, Eq. 11.22]:

$$\begin{aligned} S_{1111} &= A(1-m)(3+\gamma+m), & S_{1122} &= A(1-m)(1-\gamma-m), \\ S_{2222} &= A(1-m)(3+\gamma-m), & S_{2211} &= A(1+m)(1-\gamma+m), \\ S_{1212} &= A(1+m^2+\gamma), \end{aligned} \quad (30)$$

where $A = 1/[8(1-\nu)]$, $\gamma = 2(1-2\nu)$, and $m = (a_1 - a_2)/(a_1 + a_2)$, with a_1 and a_2 denoting the semi-axes of the ellipse \mathcal{B} . The frame $(\mathbf{e}_1, \mathbf{e}_2)$ is aligned with the principal directions of \mathcal{B} . The EMT is then evaluated by using (30) in (23).

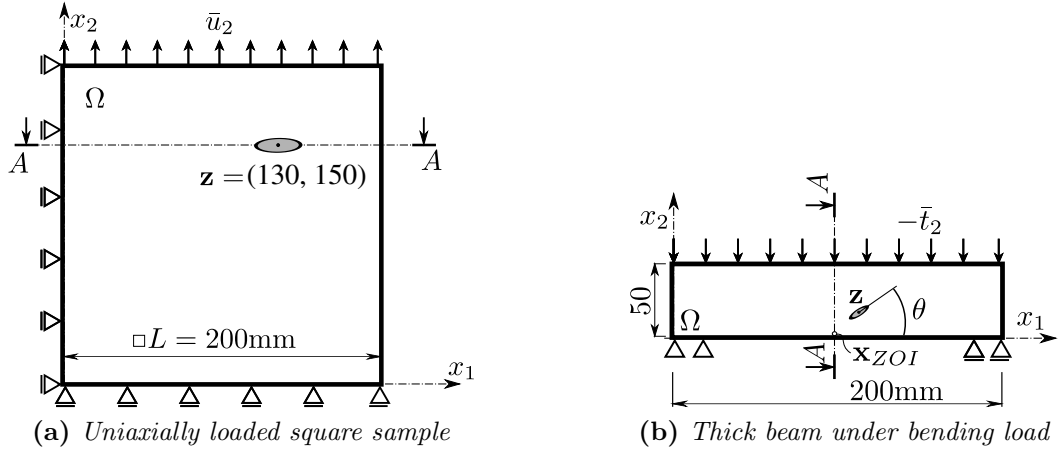


Figure 3: Geometry and boundary conditions for Example 1 (a) and Example 2 (b).

4. Numerical examples

The proposed treatment is now illustrated on two examples, each featuring a single small elliptic flaw. The first example involves a square sample under uniaxial loading (Fig. 3a), while the bending of a thick beam is considered in the second (Fig. 3b). The numerical results

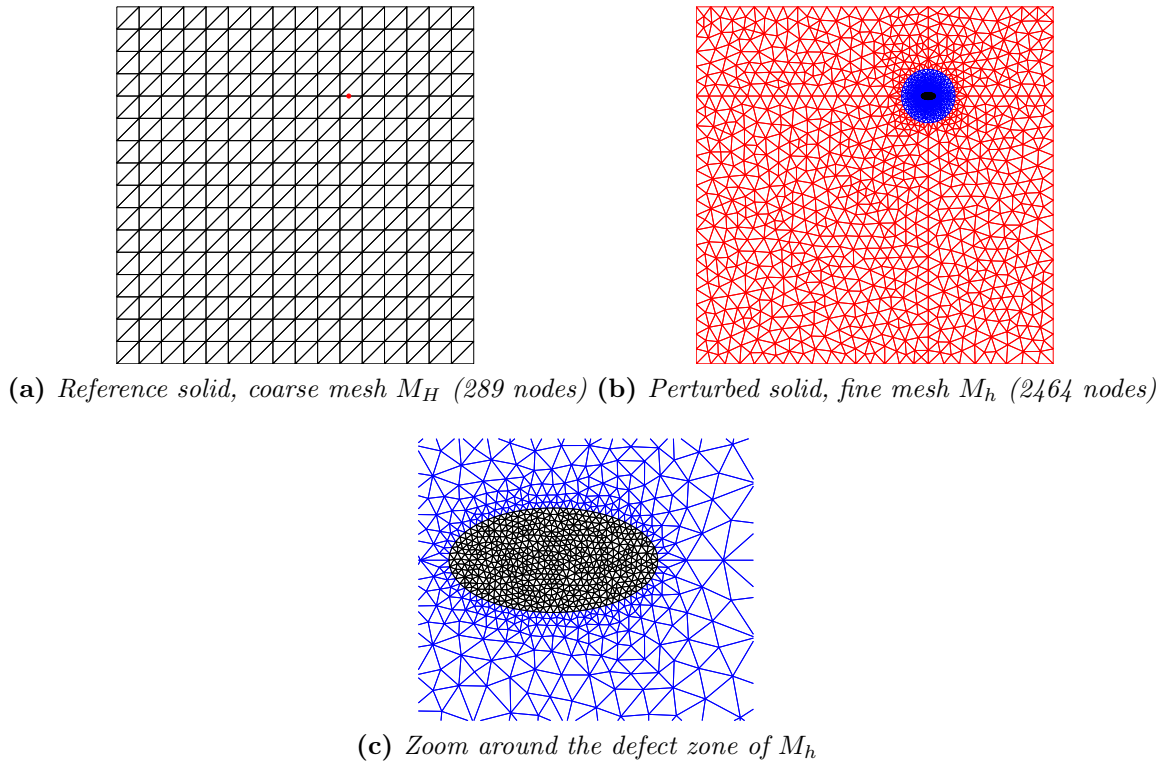


Figure 4: Finite element meshes. In mesh M_h , the disk D of radius R containing elements surrounding the defect is shown in blue, the remaining part $\Omega \setminus D$ in red.

to follow were obtained by means of the code **FEAP** [22], using meshes made of three-noded triangular elements with continuous piecewise-linear displacement interpolation.

4.1. Example 1

The coarse analysis mesh M_H (Fig.4a) is regular and features 289 nodes. In addition, a fine comparison mesh M_h (Fig.4b) modeling the inhomogeneity (i.e. entailing mesh refinement at the defect scale in a neighbourhood of B_a), featuring 2464 nodes, was set up for comparing the "brute force" solution \mathbf{u}_a^h of problem (4) to its asymptotic approximation $\tilde{\mathbf{u}}_a^H$. All finite element solutions discussed in this section (such as $\tilde{\mathbf{u}}_a^H$ or \mathbf{u}_a^h) are labelled with the characteristic element size H or h (with $h \leq H$) of the mesh used for computing them.

We first present the comparison of the computed asymptotic correction $\tilde{\mathbf{v}}_a^H$ against the reference solution \mathbf{v}_a^h , obtained on M_h as $\mathbf{v}_a^h := \mathbf{u}_a^h - \mathbf{u}^h$ (computing the background solution \mathbf{u}^h requires completing M_h with a fine mesh of the interior of B_a if the defect is a hole).

Considering a defect in the form of an elliptic inhomogeneity (with the material properties given as $E = 380000$ MPa, and $\nu = 0.18$, $E^*/E = 0.5$) with semiaxes $a_1 = 4$ mm, $a_2 = 2$ mm, Figure 5 shows contour plots of both Cartesian components of $\tilde{\mathbf{v}}_a^H$ and \mathbf{v}_a^h , which can be observed to agree well (recalling that the asymptotic correction (9) is only meaningful outside a fixed neighbourhood of B_a). In addition, $\tilde{\mathbf{v}}_a^H$ is plotted along the cross-section

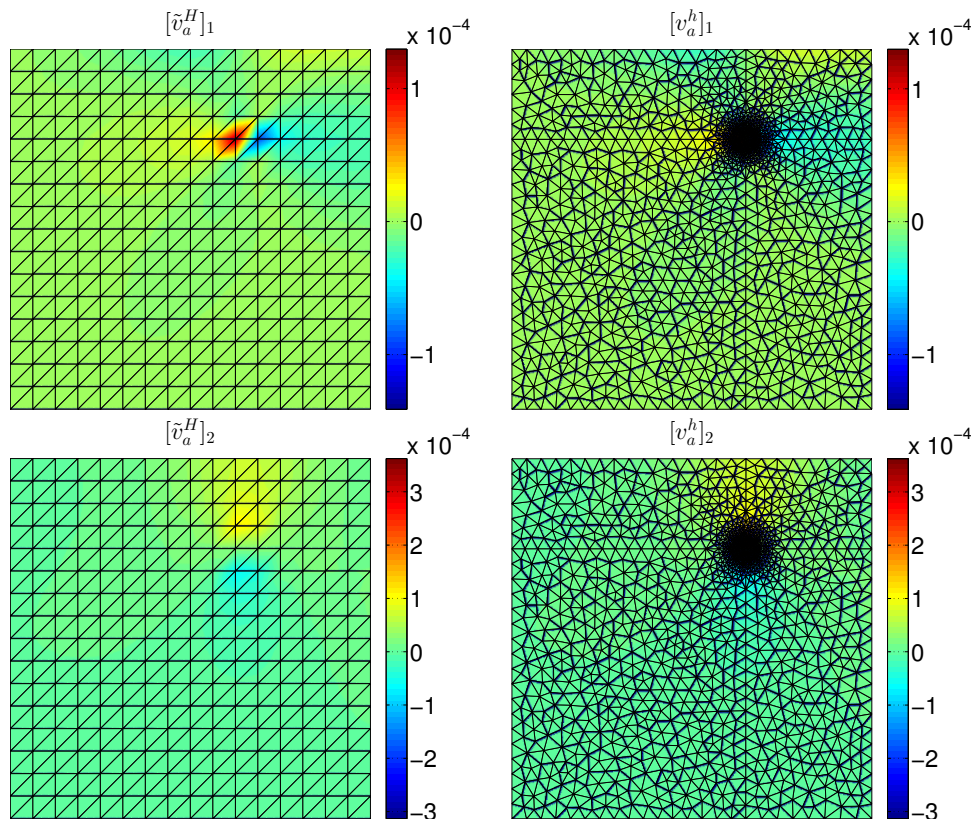


Figure 5: Contour plots of the asymptotic approximation $\tilde{\mathbf{v}}_a^H$ (left) and its reference value \mathbf{v}_a^h (right), respectively evaluated on M_H and M_h . The defect is an elliptic inhomogeneity with semiaxes $a_1 = 2$ mm, $a_2 = 1$ mm and $E^*/E = 0.5$.

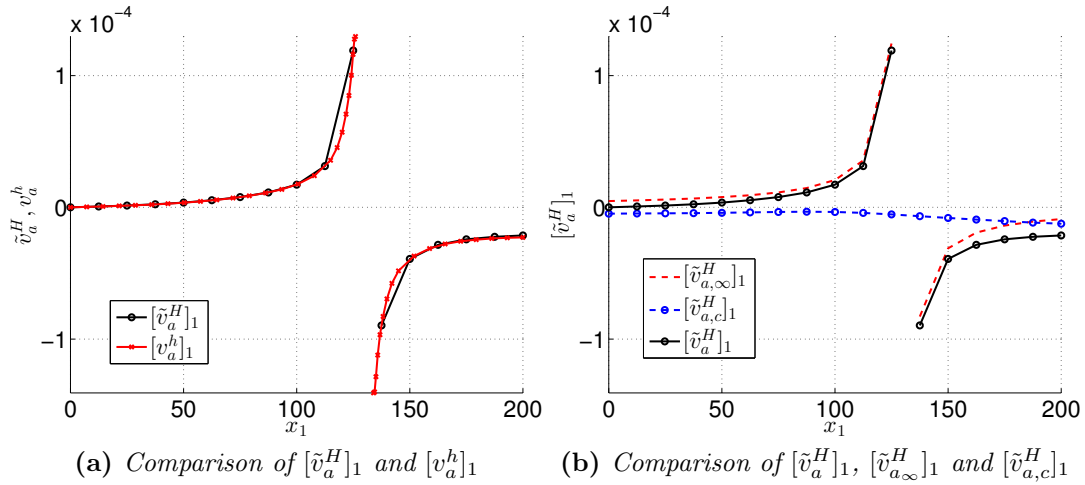


Figure 6: Plots along cross-section $A - A$.

$A - A$ defined in Fig. 3a, and compared to the reference solution \mathbf{v}_a^h (Fig. 6a) and to the contributions $\tilde{\mathbf{v}}_{a,\infty}^H$ and $\tilde{\mathbf{v}}_{a,c}^H$ (Fig. 6b). In Fig. 6a, a good agreement is again observed between the asymptotic correction $\tilde{\mathbf{v}}_a^H$ and the reference \mathbf{v}_a^h except, as expected, in a neighbourhood of the defect; in Fig. 6b, contributions $\tilde{\mathbf{v}}_{a,\infty}^H$ and $\tilde{\mathbf{v}}_{a,c}^H$ are seen to behave like the corresponding parts of the Green's tensor: $\tilde{\mathbf{v}}_{a,\infty}^H$ diverges, while $\tilde{\mathbf{v}}_{a,c}^H$ remains bounded, as $\mathbf{x} \rightarrow \mathbf{z}$.

Computing $\tilde{\mathbf{v}}_a^H$ entailed four FE solutions on M_H (one for the background problem (1), three for problems (19) with $1 \leq i \leq j \leq 2$), each requiring about .15s, while obtaining comparison solution \mathbf{u}_a^h on the fine mesh M_h required about 6.6s. While these CPU timings are all very moderate, our approach applied to this example performs about ten times faster than straightforward analyses on meshes involving the defect scale, and this relative advantage is expected to increase for similar analyses on three-dimensional configurations.

4.2. Convergence

We proceed with a numerical study of the convergence of $\tilde{\mathbf{v}}_a$ to \mathbf{v}_a as $a \rightarrow 0$. To this aim, we define a discrepancy indicator $R(a)$ between the asymptotic correction (transferred to the fine mesh M_h to enable comparisons) and the reference perturbation solution:

$$R(a) = a^{-2} \|\mathbf{v}_e\|_{L^2(\Omega \setminus D)} = a^{-2} \|\tilde{\mathbf{v}}_a^{hH} - \mathbf{v}_a^h\|_{L^2(\Omega \setminus D)}. \quad (31)$$

where $\tilde{\mathbf{v}}_a^{hH}$ is the projection of $\tilde{\mathbf{v}}_a^H$ (computed on M_H) on the fine mesh M_h through the mesh transfer operator $\boldsymbol{\varphi}^{hH}$ such that $\mathbf{w}^{hH} := \boldsymbol{\varphi}^{hH} \mathbf{w}^H$ is the interpolation on M_h of the values of \mathbf{w}^H at the nodes of M_h . In view of (9) and considering that $\partial_{(1)j}[\mathbf{G}_\infty^i](\cdot - \mathbf{z})$ can be evaluated analytically, we have :

$$\tilde{\mathbf{v}}_a^{hH} := \left(\partial_{(1)j}[\mathbf{G}_\infty^i]^h(\cdot - \mathbf{z}) - \boldsymbol{\varphi}^{hH}[\partial_{(2)j}\mathbf{G}_c^i]^H(\cdot, \mathbf{z}) \right) \mathcal{A}_{ijmn} u_{m,n}^H(\mathbf{z}) a^2. \quad (32)$$

In equation (31), $\|\mathbf{f}\|_{L^2(X)}$ denotes the $L^2(X)$ norm of a vector-valued function \mathbf{f} defined on a domain X , given by

$$\|\mathbf{f}\|_{L^2(X)}^2 := \int_X \|\mathbf{f}\|^2 dV, \quad (33)$$

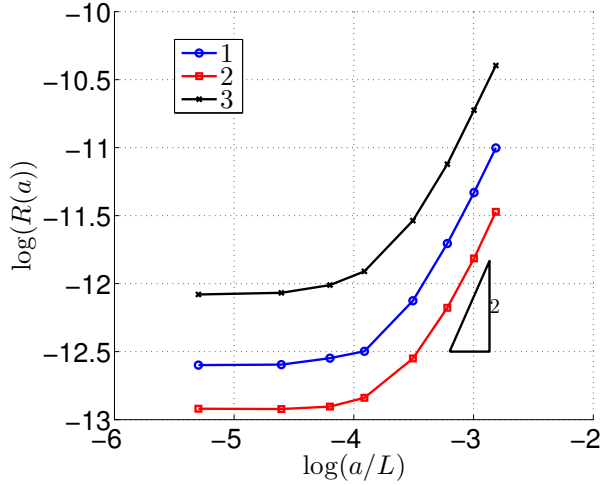


Figure 7: Plot of discrepancy $R(a)$ against the normalized inhomogeneity size. Line 1: $a_1/a_2 = 2$, $E/E^* = 2$ and $\theta = 0$; line 2: $a_1/a_2 = 2$, $E/E^* = 0.5$ and $\theta = \pi/4$; line 3: $a_1/a_2 = 1$, $E/E^* = 2$

D is a fixed neighbourhood of B_a , and the a^{-2} factor in (31) stems from the fact that $\tilde{\mathbf{v}}_a$ is the $O(a^2)$ approximation of \mathbf{v}_a in $\Omega \setminus D$. Here, D is chosen as the disk of radius R_d centered at \mathbf{z} (Fig. 4b), with R_d kept fixed as a varies.

The discrepancy $R(a)$ is plotted against a/L , the normalized characteristic size of the inhomogeneity, in Fig. 7, for several choices (given in the figure caption) of inhomogeneity shape, stiffness and orientation θ with respect to the x_1 axis. We observe that $R(a) = O(a^2)$ for not-too-small inclusion sizes ($\text{Log}(a/L) \geq -3.5$); this is the expected theoretical behaviour of $R(a)$ as $a \rightarrow 0$, as the $O(a)$ contribution to $R(a)$ is expected to vanish [23, 7] for all inhomogeneities with centrally-symmetric shape (such as ellipses). For smaller defects, the theoretical behavior of $R(a) = O(a^2)$ (which accounts only for asymptotic approximation errors) is no longer observed due to FE discretization errors becoming comparatively significant (see [24] for an analysis of the interplay between asymptotic and FE errors for the Poisson equation with Dirichlet boundary conditions).

4.3. Example 2

This example concerns the bending of a simply supported beam (of size 200×50) loaded on its top side with uniformly distributed normal load $\bar{t}_2 = -30$ MPa (Fig. 3b). The material properties are given as $E = 380000$ MPa, and $\nu = 0.18$. The inhomogeneity is taken as an elliptic hole located at $\mathbf{z} = (115, 10)$, whose major semiaxis a_1 has an inclination angle θ relative to the x_1 direction (Fig. 3b). The defect size is defined in terms of the semiaxes $a_1 = 4$, $a_2 = 2$, except where stated differently. For this bending example the perturbation caused by the inhomogeneity will be examined in terms of the stress perturbation, which is usually taken as the quantity of interest for the design of structural components. Accordingly, we will focus on the evaluation of the asymptotic approximation $\tilde{\boldsymbol{\sigma}}_a^H := \mathbf{C} : \boldsymbol{\varepsilon}[\tilde{\mathbf{v}}_a^H]$, valid except inside a neighbourhood of B_a , of the (linear elastic) stress perturbation induced by the defect, and its comparison with the reference stress perturbation $\boldsymbol{\sigma}_a^h := \mathbf{C}_a : \boldsymbol{\varepsilon}[\mathbf{v}_a^h]$.

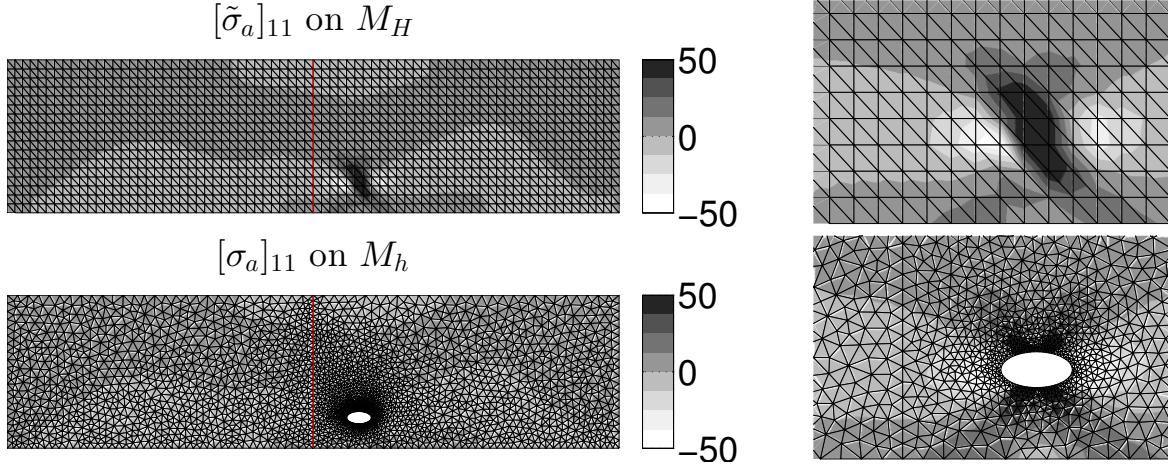


Figure 8: Contour plots of the asymptotic approximation $\tilde{\sigma}_a^H$ of the stress perturbation (upper plots) and the reference perturbation σ_a^h (lower plots). The plots on the right are zooms showing both fields in the vicinity of \mathbf{z} . The elliptic hole is located at $\mathbf{z} = (115, 10)$, and its inclination is $\theta = 0$.

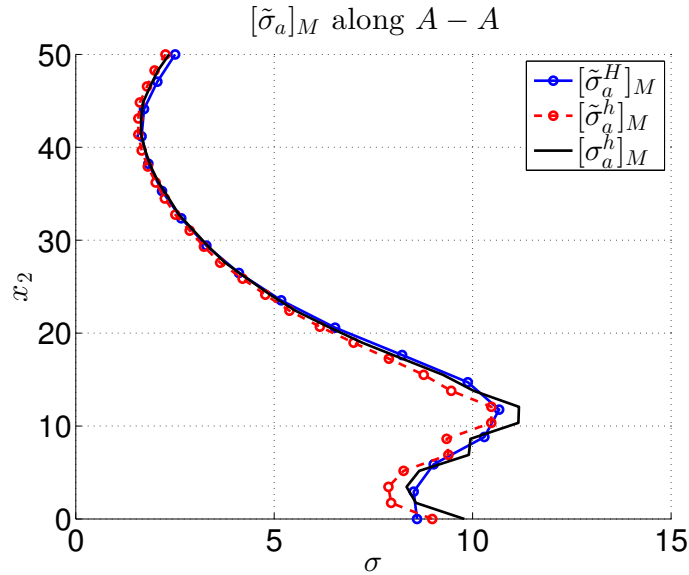


Figure 9: Comparison of the asymptotic approximation in terms of stress perturbation computed on the fine ($\tilde{\sigma}_a^h$) and coarse ($\tilde{\sigma}_a^H$) meshes against the reference perturbation σ_a^h along the cross-section $A - A$, for the inhomogeneity of Fig. 8 (lower plots), whose vertical position is $x_2 = 10$.

Both quantities are shown (in terms of their component σ_{11}) as contour plots in Fig. 8. The asymptotic stress perturbation $\tilde{\sigma}_a^H$, computed on M_H , compares well with its reference counterpart σ_a^h computed on M_h (recalling that $\tilde{\sigma}_a^H$ is not valid inside a neighbourhood of B_a , as exemplified in the blow-up views shown in Fig. 8, right). The scale $-50 \leq \sigma \leq 50$ and the colormap are chosen so as to emphasize the far field character of the outer expansion, based on (8).

We next examine von Mises equivalent stress solutions (rather than individual stress

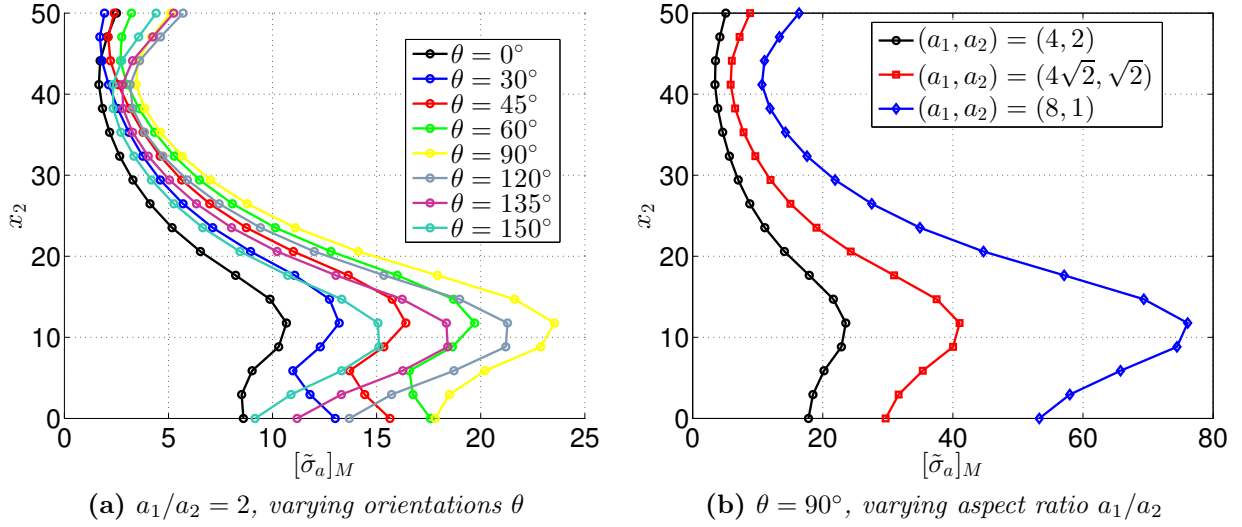


Figure 10: Asymptotic approximation in terms of the von Mises stress perturbation $[\tilde{\sigma}_a^H]_M$ along the coordinate x_2 spanning the cross-section $A - A$. The elliptic hole is located at $\mathbf{z} = (115, 10)$.

components) evaluated along the coordinate x_2 spanning the vertical cross-section $A - A$ (see Fig. 3b, also indicated in the left plots of Fig. 8). For completeness, this comparison, shown in Fig. 9, also includes the asymptotic approximation $\tilde{\sigma}_a^h$ obtained using the fine mesh M_h , which coincides with the reference mesh in $\Omega \setminus B_a$. The asymptotic approximations $\tilde{\sigma}_a^H$ (coarse) and $\tilde{\sigma}_a^h$ (fine) are seen to agree well with one another and with the reference σ_a^h .

Having verified our approach we now use the asymptotic approximation $\tilde{\sigma}_a^H$ to test the stress perturbation for various inhomogeneity orientations and shapes, searching for the hypothetical defect(s) which might be critical. This study benefits from the developed method and its main advantage: for given background and inhomogeneity properties (both being isotropic for this example) and position \mathbf{z} , we can compute stress perturbation distributions in $\Omega \setminus B_a$ for various inhomogeneity orientations, shapes and sizes (i.e. various values of θ and a_1, a_2 for this example) at almost no additional computational cost. Searching for critical defects just requires simple evaluations of EMTs for different inhomogeneity geometries.

To illustrate the procedure and possible uses of the developed method, we firstly give the evolution of the Mises stress perturbation distribution along the cross-section $A - A$ in Fig. 10 a). Here the inhomogeneity is taken as an elliptic hole (visible on the lower plots in Fig. 8), located at $\mathbf{z} = (115, 10)$, whose ratio of principal axes is $a_1/a_2 = 2$. The orientation of the elliptic hole is defined as the angular parameter θ . It is noticeable in Fig. 10 a) that for the chosen model problem with the given beam geometry, load, and shape and properties of the inhomogeneity, the orientation of $\theta = 90^\circ$ yields the highest stress perturbation along the cross-section (see yellow curve in Fig. 10a)). Thus, for the chosen defect this orientation can be deemed the most critical one. To complete this illustrative example, we now keep the orientation fixed to $\theta = 90^\circ$ and observe the influence of the inhomogeneity shape, considering three shapes defined by $(a_1, a_2) = (4, 2)$, $(4\sqrt{2}, \sqrt{2})$ or $(8, 1)$ (so that the

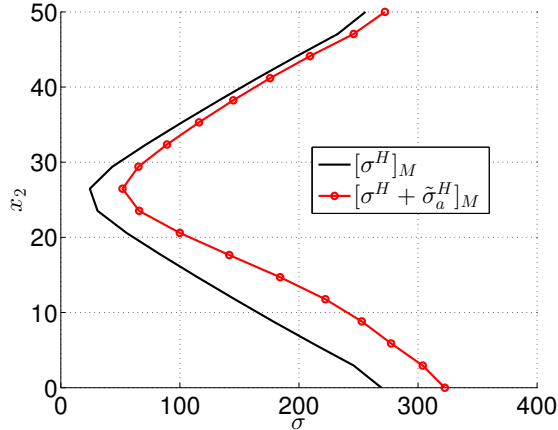


Figure 11: Comparison of the background and total stress fields along the cross-section $A-A$, for the case $a_1, a_2 = (8, 1), \theta = 90^\circ$.

defect surface area is kept fixed). The equivalent stresses for the corresponding asymptotic approximations are shown in Fig. 10b. Not surprisingly, increasing principal axes ratios (i.e. sharper defect shapes) produce higher stress perturbations. We emphasize again that such parametric studies are conducted at almost no additional computational cost.

Although results in Figs. 8 to 10 focus on the stress perturbation, criticality is expected to depend on the total stress $\sigma_a := \mathbf{C}_a : \boldsymbol{\varepsilon}[\mathbf{u}_a]$, which is using the present method approximately evaluated as $\sigma_a \approx \sigma^H + \tilde{\sigma}_a^H$, where $\sigma^H := \mathbf{C} : \boldsymbol{\varepsilon}[\mathbf{u}^H]$ is the background stress as evaluated on the analysis mesh. In Fig. 11, we show (in terms of their von Mises equivalent stress) the background and the (asymptotic approximation of the) total stress for the case $a_1, a_2 = (8, 1), \theta = 90^\circ$, noting that the latter significantly deviates from the former.

4.4. Beam bending example with varying flaw

We now illustrate the stress perturbation analysis where the flaw location \mathbf{z} varies while the evaluation point \mathbf{x} is fixed (scenario (b) of Sec. 3.2). In this case, we aim at finding the most critical location of a defect with respect to a given criterion evaluated at a fixed point of interest (given as e.g. \mathbf{x}_{ZOI} in Fig. 3). Remember that in this case we first solve the BVP (19) setting $\mathbf{z} = \mathbf{x}_{ZOI}$, and then differentiate the resulting numerical solution for $H_\ell^k(\cdot, \mathbf{x})$.

Accordingly, the contour plots of Fig. 12 show for given \mathbf{x} (taken as $\mathbf{x} = (100, 5)$) the map $\mathbf{z} \mapsto [\sigma^H(\mathbf{x}) + \tilde{\sigma}_a^H(\mathbf{x}; \mathbf{z})]_M$ of the von Mises equivalent stress of the total stress at \mathbf{x} with varying flaw locations \mathbf{z} , the flaw being taken as an elliptic hole. The first, second and third columns of Fig. 12 correspond to the semiaxes (a_1, a_2) being equal to $(4, 2)$, $(4\sqrt{2}, \sqrt{2})$, and $(8, 1)$, respectively, while the rows 1 to 4 correspond to flaw orientations θ equals to 0° , 45° , 90° , and 120° , respectively. Such plots provide a “sensitivity map” (of stress w.r.t. defect location). Similar sensitivity maps could be defined for any quantity of interest defined in terms of the total stress field, e.g. maximum equivalent stress over Ω or resulting loads.

This “inverse” approach again takes advantage of the fact that, for given background configuration and stress-based quantity of interest (here the total stress at a given location \mathbf{x}), the defect location and other characteristics can be varied at virtually no cost. The

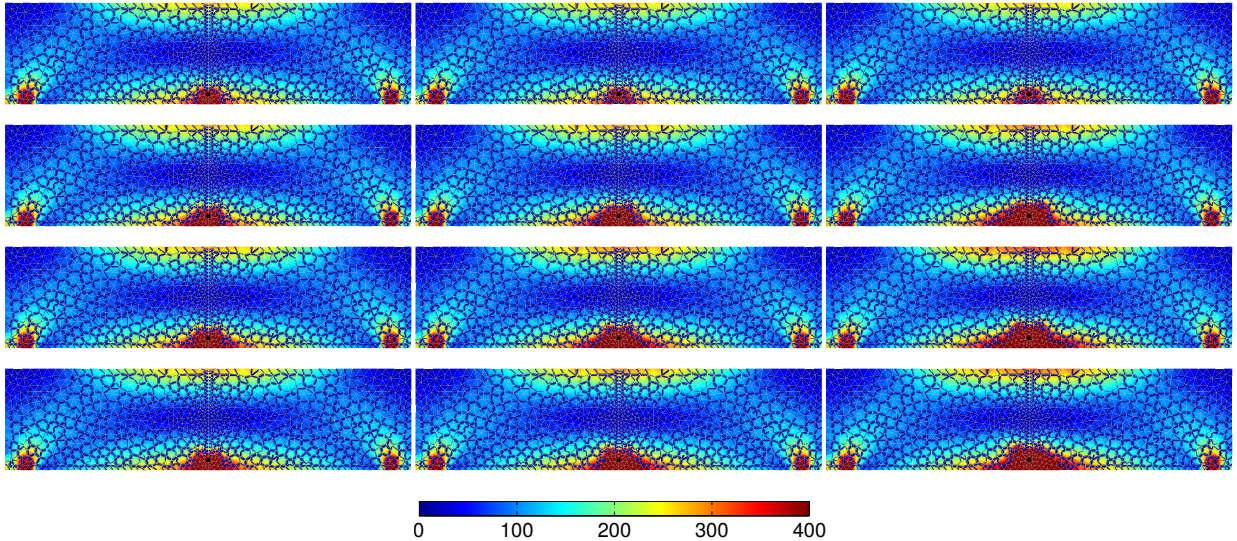


Figure 12: Contour plots of the asymptotic approximation in terms of Mises stress perturbation $[\bar{\sigma}_a]_M$ with the varying flaw \mathbf{z} , and fixed evaluation point $\mathbf{x} = (100, 5)$ denoted with $+$. The flaw is taken as elliptic hole given as follows. Semiaxes (a_1, a_2) for: column 1 - $(4, 2)$; column 2 - $(4\sqrt{2}, \sqrt{2})$; column 3 - $(8, 1)$. Orientations θ for: row 1 - 0° ; row 2 - 45° ; row 3 - 90° ; row 4 - 120° .

only difference from the "direct" approach of scenario (a) is that (21) requires the complete background strain field (rather than its value at one location).

5. Conclusion and perspectives

A numerical strategy for predicting the perturbation caused by small isolated inhomogeneities in elastic solids has been developed, implemented and demonstrated. The treatment is based on a two-scale asymptotic expansion which separates defect and structure length scales through inner and outer expansions. We focused on the structure scale, and hence on the computation of corrections based on outer expansions. Meshing the isolated inhomogeneity (with the attendant mesh preparation and computational costs) is avoided, the whole analysis relying on a mesh that is suitable for the background (i.e. defect-free) configuration. Key ingredients of the outer asymptotics-based correction, namely Green's tensors and elastic moment tensors, were presented and the details about their computation given. The two numerical examples show satisfactory behavior in terms of accuracy, convergence (with small defect size) and flexibility (for inexpensive parametric studies).

The next steps of this work include (i) matching the inner and outer asymptotic expansions to obtain uniform expansions, (ii) applying the developed strategy to assess the criticality of defects by considering virtual micro-defects and varying their positions, sizes and mechanical properties, and in particular (iii) incorporate randomness of micro-defect characteristics in such analyses. Criticality assessment will thus be greatly aided by the ability of conducting comprehensive parametric studies for varying flaw types, locations, orientations and characteristics. Defect randomness can for example affect products output

by many manufacturing processes, e.g. casting (where defects such as porosities, heterogeneities and cavities are expected, see e.g. [8]) or welding (creating defects such as cracks, gas holes, hydrogen inclusions and porosities, see e.g. [9]). Addressing these real-life problems for which the homogenization techniques do not apply is a long-term perspective of the proposed asymptotics-based numerical strategy.

Acknowledgement

The authors are funded by ANR through project ARAMIS (ANR 12 BS01-0021).

References

- [1] M. Dambrine, G. Vial, A multiscale correction method for local singular perturbations of the boundary, *ESAIM:M2AN* 41 (2007) 111–127.
- [2] D. Brancherie, M. Dambrine, G. Vial, P. Villon, Effect of surface defects on structure failure: a two-scale approach, *Eur. J. Comput. Mech.* 17 (2008) 613–624. doi:10.3166/remm.17.613-624.
- [3] V. Bonnaillie-Noël, D. Brancherie, M. Dambrine, S. Tordeux, G. Vial, Effect of micro-defects on structure failure coupling asymptotic analysis and strong discontinuity, *Eur. J. Comput. Mech.* 19 (2010) 165–175. doi:10.3166/ejcm.19.165-175.
- [4] M. Silva, P. H. Geubelle, D. A. Tortorelli, Energy release rate approximation for small surface-breaking cracks using the topological derivative, *J. Mech. Phys. Solids* 59 (2011) 925–939.
- [5] A. A. Novotny, J. Sokolowski, *Topological derivatives in shape optimization*, Springer, 2012.
- [6] M. Bonnet, G. Delgado, The topological derivative in anisotropic elasticity, *Quart. J. Mech. Appl. Math* 66 (2013) 557–586.
- [7] M. Bonnet, R. Cornaggia, Higher order topological derivatives for three-dimensional anisotropic elasticity, *ESAIM: Math. Modell. Numer. Anal.* (2017) in press.
- [8] D. Mery, T. Jaeger, D. Filbert, A review of methods for automated recognition of casting defects, *Insight: Non-Destructive Testing and Condition Monitoring* 44 (7) (2002) 428–436.
- [9] G. Wang, T. Liao, Automatic identification of different types of welding defects in radiographic images, *NDT & E International* 35 (8) (2002) 519 – 528. doi:10.1016/S0963-8695(02)00025-7.
- [10] T. Mura, *Micromechanics of Defects in Solids*, Martinus Nijhoff Publishers, 1987.
- [11] H. Ammari, H. Kang, G. Nakamura, K. Tanuma, Complete asymptotic expansions of solutions of the system of elastostatics in the presence of an inclusion of small diameter and detection of an inclusion, *J. Elast.* 67 (2) (2002) 97–129. doi:10.1023/A:1023940025757.
- [12] H. Ammari, H. Kang, *Polarization and moment tensors: with applications to inverse problems and effective medium theory*, Springer, 2007.
- [13] H. Ammari, H. Kang, K. Kim, H. Lee, Strong convergence of the solutions of the linear elasticity and uniformity of asymptotic expansions in the presence of small inclusions, *J. Differ. Equations* 254 (2013) 4446–4464.
- [14] S. A. Nazarov, J. Sokolowski, M. Specovius-Neugebauer, Polarization matrices in anisotropic heterogeneous elasticity, *Asymptot. Anal.* 68 (2010) 189–221.
- [15] S. Amstutz, A. Bonnafé, Topological derivatives for a class of quasilinear elliptic equations, *J. Math. Pures Appl.* 107 (2017) 367–408.
- [16] V. Maz'ya, S. A. Nazarov, B. A. Plamenevskii, *Asymptotic theory of elliptic boundary value problems under a singular perturbation of the domains (vols. 1 and 2)*, Birkhäuser, 2000.
- [17] E. Beretta, E. Bonnetier, E. Francini, A. L. Mazzucato, Small volume asymptotics for anisotropic elastic inclusions, *Inverse Problems in Imaging* 6 (2011) 1–23.
- [18] J. D. Eshelby, The determination of the elastic field of an ellipsoidal inclusion and related problems, *Proc. R. Soc. Lond. A* 241 (1957) 376–396.

- [19] V. I. Lebedev, D. N. Laikov, A quadrature formula for the sphere of the 131st algebraic order of accuracy, *Doklady Mathematics* 59 (3) (1999) 477–481.
- [20] C. A. Brebbia, J. C. F. Telles, L. C. Wrobel, *Boundary element techniques*, Springer, 1984.
- [21] M. Bonnet, *Boundary integral equation methods for solids and fluids*, John Wiley and Sons, Inc, 1999.
- [22] R. L. Taylor, FEAP - finite element analysis program (2014). <http://www.ce.berkeley/feap>
- [23] M. Bonnet, Higher-order topological sensitivity for 2-D potential problems. application to fast identification of inclusions, *Int. J. Solids Struct.* 46 (2009) 2275–2292.
- [24] L. Chesnel, X. Claeys, A numerical approach for the poisson equation in a planar domain with a small inclusion 56 (2016) 1237–1256.